Lithiophilic Mo₃N₂/MoN as Multifunctional Interlayer for Dendrite-Free and Ultra-Stable Lithium Metal Batteries

Xiaojuan Zhang[a, b], Yuanfu Chen*[a, c], Katam Srinivas[a], Bo Yu[a], Fei Ma[a], Bin Wang[a], Xinqiang Wang[a], Jiarui He*[a], Zheng-Long Xu*[b]

[a]School of Electronic Science and Engineering, and State Key Laboratory of Electronic Thin Films and Integrated Devices, University of Electronic Science and Technology of China, Chengdu 610054, PR China

[b]Department of Industrial and Systems Engineering, The Hong Kong Polytechnic University, Hong Kong SAR, PR China

[c]School of Science, and Institute of Oxygen Supply, Tibet University, Lhasa, 850000, PR China

*Corresponding authors

E-mail: yfchen@uestc.edu.cn (Y. F. Chen)

E-mail: zhenglong.xu@polyu.edu.hk (Z. L. Xu)

E-mail: hejiarui123@sina.com (J. R. He)

Abstract: The formation of lithium dendrite and the unstable electrode/electrolyte interface, especially at high rates, are the dominant obstacles impeding the implementation of lithium metal batteries (LMBs). To tackle these fundamental challenges, here we propose a lithiophilic Mo_3N_2/MoN heterostructure (designated as MoN_x) interlayer for dendrite-free and ultra-stable lithium metal anodes for the first time. The MoN_x interlayer presents excellent electrolyte wettability, fast lithium diffusion kinetics and strong mechanical strength, which function synergistically to inhibit lithium dendrite growth. During cycling, an in-situ formation of Li_3N-rich solid electrolyte interphase layer and metallic Mo phase can regulate the Li-ion conductivity and Li metal deposition, thus indicating uniform and compact Li plating. Above ameliorating features accompany an ultra-long-life of 2000 hours at a high current density of 5 mA cm^{-2} for the MoN_x-Li anode. The feasibility of the MoN_x-Li anode in LMB is further confirmed in conjunction with $LiFePO_4$ cathodes. The full cells deliver exceptionally high-capacity retentions of above 82.0% after 500 cycles at 1C and 425 cycles at 3C, which are among the best thus far reported for LMBs. This work provides both new insights towards functional interlayer design and effective transition-metal nitrides for practical LMBs.

Keywords: Lithium metal battery, Mo_3N_2/MoN heterostructure, DFT calculations, *in-situ* reaction, Li_3N-rich layer

1. Introduction

With the increasing demand of portable electronic devices and electric vehicles, the development of advanced energy storage systems with high energy density becomes imperative [1-5]. To obtain higher energy density than what the current Li-ion batteries with graphite anode can offer, a straightforward strategy is to explore anode materials with high theoretical capacities and low redox potentials [6-10]. Thanks to its extremely high theoretical capacity of 3861 mAh g^{-1} and the lowest reductive potential of -3.04 V vs. standard hydrogen electrode (SHE) among all the potential anodes, Li metal has been considered ideal for the next-generation lithium battery, named as lithium metal batteries (LMBs) [11-15]. However, the practical implementation of LMBs is greatly hindered by several fundamental challenges, including the large volume expansion of Li metal, unstable solid electrolyte interphase (SEI), and lithium dendrite growth, leading to porous and incompact lithium deposition [16], continuous consumption of electrolytes [17, 18], puncture of separator, and eventually the failure of LMBs [19].

To address the above obstacles, many strategies have been proposed over the past decade, including the electrolyte optimization, functionalized separator, construction of three-dimensional current collectors and building artificial SEI layers [6, 20-24]. In general, an organic/inorganic passivation SEI layer would inevitably generate on the surface of Li metal due to the higher Fermi level of Li metal than the lowest unoccupied molecular orbital (LUMO) levels of almost all organic electrolytes [6]. The native SEI is inhomogeneous and mechanically weak, which accelerates the Li dendrite growth by inducing concerted electric field and localized Li ion flux [6]. It is therefore essential to engineer artificial SEI with specific properties to suppress the aggressive dendrite growth and electrolyte/electrode side reactions [18, 25, 26]. An optimal artificial layer should possess strong

mechanical strength to accommodate the stress of Li dendrite [27] as well as lithiophilic characteristic to guide the uniform deposition of Li metal [28]. To this end, lots of surface coating materials have been prepared, e.g. PMMA/PVDF coated Li [18], GZCNT-coated Li [29], OIHL coated Li [30], and β-PVDF coated Li [31] with improved cyclic stability of Li metal. A representative example is reported by Dasgupta's group [32] who deposited Al_2O_3 on Li metal by chemical vapor deposition method. The symmetric cells of Al_2O_3 coated Li anode retained 1259 cycles before failure. Another protective layer of Li_3N was also deposited by N_2 plasma activation of the Li metal [33], which symmetric cells exhibited stable voltage profiles for 500 h at 0.5 mA cm^{-2} and 1 mAh cm^{-2}. Despite the enhanced electrochemical performance, these methods or protective layers are difficult to be scale-up for practical applications due to the elaborative experimental processes and expensive apparatus. Few reported protective layers can meet all the requirements as aforementioned for practical LMBs. Therefore, how to construct an artificial interface with multifunction (e.g., admirable mechanical properties, high interface energy and excellent lithiophilicity) using a facile and propagable method that can lead to dendrite-free and ultra-stable LMBs still remains a great challenge. Currently, the heterostructural functional materials have attracted significantly attention due to the heterostructural interfaces with a high diffusion coefficient enabling rapid ion diffusion flux [34]. Therefore, heterostructure materials have been developed as an available way to improve reaction kinetics through the effect of built-in electric field, which is better ion diffusion kinetics than pure materials [35]. Furthermore, the heterostructure with the abundant phase boundaries can accelerate the solid-state diffusion and contributing notable pseudocapacitive effects, leading to improved rate performance [36]. Specifically, some heterostructure composites materials can be converted from semiconducting to metallic after alkali-metal mineralization, which can provide the

deposition sites and overcome the issues of poor conductivity [37-39]. Hence, proper construction heterostructure materials is believed to be effective to significantly improve the electrochemical performance for advanced alkali metal battery.

Herein, for the first time, we develop a heterostructural, lithiophilic and multifunctional Mo_3N_2/MoN (designated as MoN_x) nanobelt as interlayer for exceptionally stable Li anodes (denoted as MoN_x-Li) by a simple drip coating method. The novel MoN_x heterostructural interface presents favorable electrolyte wettability, strong mechanical strength, and high surface energy, which can effectively inhibit the lithium dendrite growth. In addition, a lithiophilic and ionically super conductive Li_3N-rich SEI layer is formed from MoN_x during the Li plating/stripping processes, which can modify the rapid Li migration and induce homogeneous Li ion flux. Meanwhile, a metallic Mo phase is also generated by reduction of MoN_x, which provides abundant sites for Li deposition via the strong Li–Mo interactions, thus indicating the uniform deposition of Li metal. These interesting findings are demonstrated by theoretical and experimental investigations. Consequently, symmetric cells of the MoN_x-Li metal anode exhibit excellent cyclic stability for over 2000 h with small hysteresis voltages of ~65 mV at high current of 5 mA cm^{-2} and capacity of 1 mAh cm^{-2}. For LMBs application, the MoN_x-Li//Li iron phosphate (LFP) full cell delivers a remarkable capacity retention of 82.3% at an extremely high rate of 3C after 425 cycles. These values are among the best thus far reported for LMBs, promoting their practical applications with high-capacity Li metal anodes.

2. Experimental Section

2.1 Synthesis of heterostructural Mo₃N₂/MoN nanobelt

Ammonium molybdate (($NH_4)_2MoO_4$) and HNO_3 were analytical grade and purchased from

Chengdu Chemical Reagent Factory (Chengdu, China). MoN was purchased from Tianjin Solomon Biological Technology Co., LTD (Tianjin, China). N-methylpyrrolidone (NMP) was electronic grade and purchased from Sichuan Xieli Biochemical Reagent Co., LTD (Chengdu, China). LiFePO$_4$ (LFP) were 98% purity and purchased from Beijing Huawei Ruike Chemical Co., LTD (Beijing, China). The water used throughout the experiment was doubly distilled water (H$_2$O).

1.4 g of (NH$_4$)$_2$MoO$_4$ was dissolved in a 70 mL of acidified water (10 mL of 65% HNO$_3$) under constant stirring at ambient temperature for 1 h. Subsequently, the resulting reaction mixture was transferred to a Teflon-lined reactor and subjected to hydrothermal reaction (200 °C for 24 h). After cooling down to ambient temperature, the solid MoO$_3$ nanobelt obtained was washed by ethanol and distilled H$_2$O. The as-obtained MoO$_3$ nanobelt evenly placed in a crucible and annealed to 750 °C for 6 h (with 5 °C min^{-1} heating rate) under flowing ammonia gas (100 sccm) and the obtained sample was established to be the heterostructural Mo$_3$N$_2$/MoN nanobelt (denoted as MoN$_x$).

2.2 Fabrication of MoN$_x$-Li anode

The heterostructural MoN$_x$ nanobelt protected Li anodes (MoN$_x$-Li) have been prepared by drop casting method. Typically, the homogeneous mixture of MoN$_x$ nanobelt and PVDF with the mass ratio of 9:1 was dried for 2 h at 100 °C in a vacuum drying oven before being moved to the Argon gas filled glove box. Afterwards, it was dispersed in *N*-Methyl pyrrolidone (NMP) with a concentration of 0.3 wt.% under constant stirring for 12 h and then sonicated (1 h) for sealed dispersion, followed by dripping the suspension (200 μL) onto the Li foil (the mass loading of 0.5 mg cm^{-2}) by a pipette and were dried using a hot plate at 50 °C for 12 h. Finally, the heterostructural MoN$_x$ protected Li anodes (marked as MoN$_x$-Li) were obtained. The preparation of MoN protected Li anode (marked as MoN-Li) is similar to that of MoN$_x$ protected Li anodes except that MoN$_x$ is

replaced by MoN.

2.3 Materials characterization

Field-emission scanning electron microscope (FEI Inspect F50) was used to realize the morphologies of Li metal, MoN_x, and MoN_x-Li operated at 10 kV. Transmission electron microscopy (TEM 2010F) has been employed to explore the microstructures and element distributions in MoN_x. The crystalline phases, purity and composition of MoN_x samples were elucidated by X-ray diffraction technique (XRD, Bruker D8 Advanced instrument, radiation source is Cu-Kα). X-ray photoelectron spectroscopy (XPS, Kratos Axis-Ultra Dld) was used to check the existence of elements and their surface chemical states in MoN_x. Brunauer-Emmett-Teller (N_2 adsorption/disorption isotherm, 3H-2000PM2 gas sorption analyzer) analytical technique was performed at 70 °C in order to understand the porous nature and specific surface area availability in MoN_x. Nano-indentation test of MoN_x was conducted on Bruker Hysitron TI980 to test the mechanical strength of MoN_x protective layer.

2.4 Electrochemical measurement

Standard 2025 type coin cells have been assembled the in an Argon-filled glove-box and 1 M LiTFSI (lithium bis(trifluoromethane) sulfonamide in 1:1 volume ratio of 1,3-dioxolane/1,2-dimethoxyethane (DOL/DME) with 1.0 wt.% $LiNO_3$) was used as an electrolyte for the tests of symmetric cell. Additionally, a polypropylene film Celgard 25 00 separator was used throughout the experiment. Ø16 mm Li discs (MoN_x-Li, MoN-Li or bare Li) have been utilized to fabricate the coin-type symmetric cells and are used as both cathode and anode. As mentioned above, LiTFSI was used as an electrolyte (80 µL), and the Celgard 2500 PP was used as a separator. Neware testing system (Neware battery cycler, CT-4008-5V10mA-164) was used to cycle the symmetric cells in

galvanostatic mode at diversified current densities (ranging from 2 to 5 mA cm^{-2}) during the long-term cycling stability test. Electrochemical Impedance Spectroscopy (EIS) analysis was conducted on the cells before and after 100 cycles at the open circuit potential with $10^{-1} \sim 10^5$ Hz frequency range, using 5 mV AC potential amplitude. The Li electrodes after cycling operation have been washed with DME and DOL solvents in the glovebox and transferred to the SEM chamber in order to realize the morphology analysis during the cycling process.

Mass ratio of 8:1:1 of LiFePO$_4$ (LFP), super C, and polyvinylidene fluoride (PVDF) were mixed together with NMP solvent in order to make a homogeneous slurry, and followed by subsequent coating on Al foil to fabricate the cathode electrode for full cells. Afterwards, the slurry coated Al foil were dried in a vacuum oven for 12 h at 60 °C. Thereafter, the Li//LFP and MoN$_x$-Li//LFP batteries have been subjected to galvanostatic cycled within $2.5 \sim 4.2$ V (vs. Li$^+$/Li) at different rate. The real mass loading of the LFP on electrode was approximately 5.0 mg cm^{-2}. The electrolyte employed in full cells was 1.0 M LiPF$_6$ in 1:1 volume ratio of ethylene carbonate/diethyl carbonate (EC/DEC) (Suzhou DoDoChem Technology Co., Ltd.).

3. Results and Discussion

3.1 Preparation and characterization of MoN$_x$ interlayer

In this work, the heterostructure MoN$_x$ functional material was synthesized by ammonization of MoO$_3$ nanobelt. First, the MoO$_3$ nanobelt precursor was synthesized by hydrothermal method (**Figure S1**) (see details of the experimental procedure and XRD patterns of MoO$_3$ in **Figure S2a** in Supporting Information) and exhibits a similar white color to the literature [40]. Then, the MoO$_3$ nanobelts were converted into molybdenum nitrides (MoN$_x$) by ammonization treatment. The resultant exhibits dominant peaks at 37.4°, 43.4°, 63.1°, and 75.6° referring to the (111), (200), (220)

and (311) fringe planes of Mo_3N_2 (JPCDS#89-3712), and the subsidiary peaks at 31.8°, 36.1°, 48.8°, and 64.8° are ascribed to MoN (JPCDS#89-5024) (**Figure 1a and Figure S2b**). The morphological structure of the MoN_x was evaluated by scanning electron microscopy (SEM) and transmission electron microscopy (TEM). The SEM image of MoN_x (**Figure 1b**) and pure MoN (**Figure S2b**) shows uniform nanobelt shape with average width of 210 nm and irregular granular-shape, respectively. A close observation of the MoN_x nanobelt by TEM (**Figure 1c-d**) exhibits a porous structure, possibly arising from the removal water molecules and the strain release caused by lattice mismatch during the anion exchange process of ammonization [41, 42]. The porosity was also quantitatively analyzed by Brunauer-Emmett-Teller (BET) (**Figure S3**, Supporting Information), indicating a moderate surface area of 37.76 m^2 g^{-1} and average pore sizes of 3-10 nm, consistent with the TEM observations (**Figure 1c-d**). It is worth noting that the abundant nanopores and nanobelt structure can amplify the activation areas and decrease local current density [43], suppressing the Li dendrite formation during cycling. From HRTEM images (**Figure 1e**), we clearly observe the twin-born Mo_3N_2/MoN with a *d*-spacing of 0.238 nm referring to (111) lattice of Mo_3N_2 and 0.285 nm for the (002) plane of MoN, in agreement with the XRD result (**Figure 1a**). The high-angle annular dark-field (HAADF) TEM image (**Figure 1f**) and the corresponding elemental mappings (**Figure 1g-i**) indicate the homogeneous distribution of Mo and N elements, suggesting uniform Mo_3N_2 and MoN nanocrystals in the nanobelts.

The chemical composition of MoN_x was investigated by X-ray photoelectron spectroscopy (XPS). The deconvoluted N 1s spectrum displays three peaks (**Figure 1j**) located at 400.8 eV, 398.8 eV, 397.7 eV, and 395.4 eV, which can be assigned to the pyrrolic N [44, 45], pyridinic N [44], Mo-N bond [46], and Mo $3p_{3/2}$ [47, 48], respectively. The deconvoluted Mo 3d spectrum can be assigned into

three doublet signals (**Figure 1k**). Specifically, the doublet peaks centered at 229.6/232.6 eV and 228.8/231.9 eV are assigned to the Mo-N bonds of MoN and Mo_3N_2, respectively [49-53]. The third pair of peaks at 233.6/235.8 eV is attributable to the Mo^{6+} state, possibly originating from the oxide layer on the MoN_x surface when exposed to air [54-56]. The above intensive characterizations clearly demonstrate the successful preparation of MoN_x heterostructures, which will be utilized to modify Li metal in the following discussion.
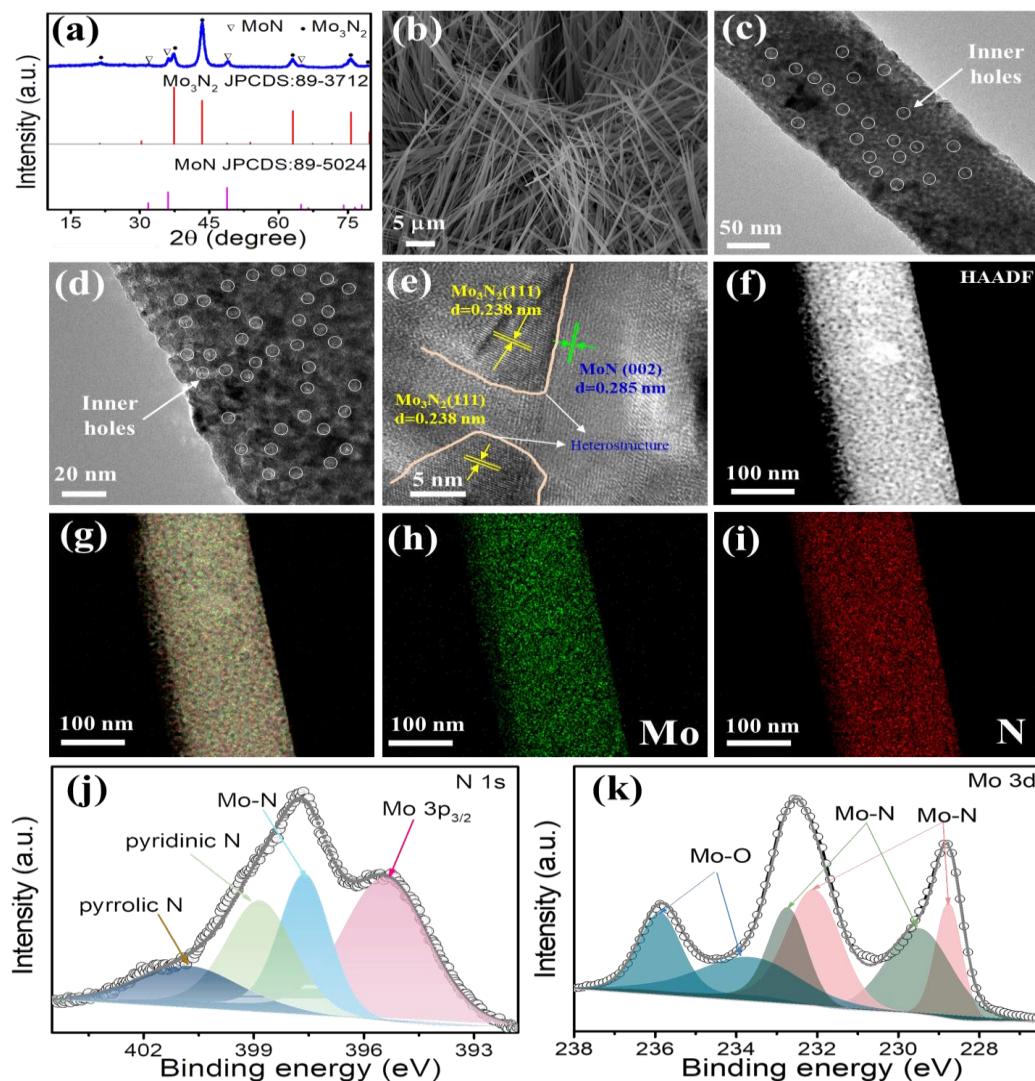

Figure 1 Synthesis and characterization of the MoN_x interlayer. XRD pattern (a), SEM image (b), TEM images (c, d), HR-TEM image (e), HAADF image (f) of MoN_x. Elemental mappings of Mo, and N elements in the MoN_x (g-i), the N 1s (j), and Mo 3d (k) XPS spectrum of MoN_x.

The homogeneous MoN_x mix slurry was coated on Li metal surface to fabricate a uniform MoN_x protective interlayer (**Figure S4**, Supporting Information) in an Ar-filled glovebox. The thickness of the MoN_x skin on Li metal surface was controlled as thin as 3.5 μm determined by the cross-sectional SEM characterizations (**Figure S5**, Supporting Information). The electrolyte wettability, surface free energy and mechanical robustness are critical indicators to estimate the quality of an artificial interlayer, to be elucidated as following. The electrolyte wettability of MoN_x interlayer was studied by dripping an electrolyte droplet on the bare Li and MoN_x-Li pellets for contact observation (**Figure S6**, Supporting Information). Interestingly, the electrolyte rapidly spread on MoN_x-Li anode, while it maintained collective on bare Li metal, indicating the superior electrolyte wettability of MoN_x-Li. The surface free energy of MoN_x-Li was then calculated by testing the polarity/non-polarity components of liquid/interlayer contact angles according to the OWRK equation and Young's equation (see details in **Table S1** and **S2** in Supporting Information). According to a surface nucleation growth model, Li metal has low surface energy and high diffusion barrier, which is detrimental to cause the lithium dendrite growth in bare Li anodes [57, 58]. It was found that the MoN_x protective interlayer presents high surface free energy of 64.36 mJ m^{-2} (**Table S3**, Supporting Information), which is of importance to uniform deposition of Li metal anode. The high surface energy together with the excellent electrolyte wettability of MoN_x layer highly promise the uniform deposition of Li metal in real batteries [57].

Li metal is recognized ductile and soft with a yield strength of 0.65 MPa [59, 60]. It means the Li dendrite can be easily deformed upon applying a small pressure [61]. Thus, coating high-modulus protective interlayers on the soft Li metal is expected to effectively prevent Li dendrite pricking the separator. The mechanical strength of the MoN_x interlayer was measured by nano-indentation

technique using a MoN_x film of 34 μm in thickness (**Figure S7**, Supporting Information). The MoN_x exhibits a hardness of about 6 MPa and a Young's modulus between 45 and 65 MPa, which is several orders of magnitude higher than the 0.65 MPa for Li dendrite. Therefore, it is reasonable to assume that mechanically strong interlayer can accommodate the pressure from Li dendrite, thus preventing the puncture of separator and internal short circuit to happen in cycling LMBs. Overall, our systematic characterizations signify highly reversible and dendrite-free Li-MoN_x anodes to be achievable.

3.2 Electrochemical performance of MoN_x-Li anodes

The electrochemical performance of MoN_x-Li anode was first investigated by using symmetric cell configuration in 1 M LiTFSI in DOL/DME (1.0 wt.% $LiNO_3$) electrolyte. When cycling at 2 mA cm^{-2} and 1 mAh cm^{-2} (**Figure 2a**), MoN_x-Li cells signified a relatively high overpotential of ~50 mV at the first 100 cycles, and gradually decreased and stabilized at 11 mV up to 1300 hrs. This interesting phenomenon is possibly owing to the high interfacial impedance of MoN_x-Li anode at the early stage, and the gradually *in-suit* formation of highly ionic conductive Li_3N and metallic Mo phases alleviated the interfacial resistances during cycling [18] to be illuminated later. In contrast, rapid and continuous increase in overpotential was observed for bare Li//Li symmetric cells under the same measurement conditions. After 800 h, the overpotential of bare Li//Li violently reached up to 291.1 mV, which is more than 25 times of the 11.4 mV for MoN_x-Li symmetric cell. The high overpotential of cycled bare Li//Li is allocated to the continuous parasitic reactions on the electrode/electrolyte interface during cycling [62]. To further verify the superior stability of MoN_x-Li anodes, the two kinds of symmetric cells were also cycled at a high current density of 5 mA cm^{-2} and a cycling capacity of 1 mAh cm^{-2} (**Figure 2b**). The MoN_x-Li symmetric cells exhibited

remarkable stability more than 2200 h with stabilized overpotentials ranging from 80 to 65 mV (see inset of **Figure 2b**), which is dramatically lower than the 485 mV for bare Li cells cycled for 360 h. Similarly, the MoN_x-Li cells were also stably cycled at 5 mA cm^{-2} and 2 mAh cm^{-2} for 1300 h (**Figure S8**, Supporting Information). In contrast, the MoN-Li symmetric cells exhibit higher overpotentials than that of MoN_x-Li symmetric cells and lower overpotentials than that of bare Li//Li symmetric cells (**Figure S9**, Supporting Information). Above comparisons indicate the decreased overpotential of MoN_x-Li cells to their bare Li and MoN-Li counterparts (**Figure S10**, Supporting Information).

The rate performances of bare Li, and MoN_x-Li symmetric cells were measured at current densities of 1, 2, 4, and 8 mA cm^{-2} for 0.5 h (**Figure S11,** Supporting Information). Compared with bare Li cell, MoN_x-Li cell exhibits much smaller voltage hysteresis at the same discharge rates. Moreover, at the initial 50 cycles of plating/stripping cycles, the overpotential of bare Li cell continuously increases due to the unstable SEI layer, accumulation of dead Li, and aggressive growth of lithium dendrite, while the MoN_x-Li cells maintain small overpotentials and steady voltage plateaus, benefiting from the MoN_x protective layer. To estimate the standing of current MoN_x-Li anode among its peers, **Table S4** (Supporting Information) summarizes the cyclic performance of Li anodes with different coatings or treatments. It is observed that the MoN_x-Li outperforms all its peers in cycle life under a high current density of 5 mA cm^{-2}, which is of essential importance to realize fast-charging LMBs with high safety.
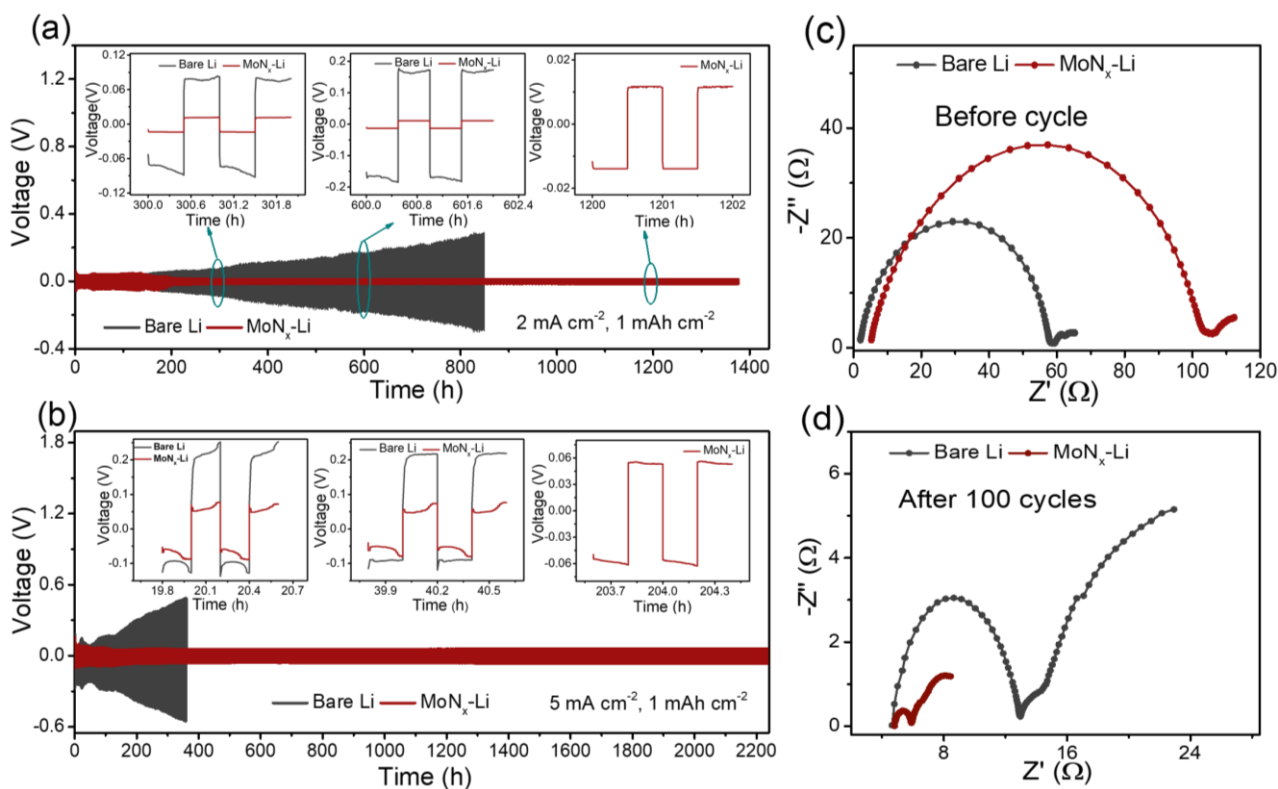
Figure 2 Electrochemical performance of bare Li and MoN_x-Li symmetric cells. Comparison of the cycling stabilities of Li//Li and MoN_x-Li//MoN_x-Li symmetric cell with the cycle capacity of 1 mAh cm^{-2} at 2 mA cm^{-2} (a) and 5 mA cm^{-2} (b), the insert of corresponding cycle profiles at different cycles; Nyquist plots of Li//Li and MoN_x-Li//MoN_x-Li symmetric cell before (c) and after (d) 100 cycles under 2 mA cm^{-2} with a cycle capacity of 1 mAh cm^{-2}.

Electrochemical impedance spectroscopy (EIS) measurements of the bare Li and MoN_x-Li symmetric cells before and after cycling were conducted to illuminate the reaction kinetics and interfacial evolution during cycling. In **Figure 2c** and **Figure S12a**, the Nyquist plot of the fresh MoN_x-Li and MoN-Li cell exhibits a larger semicircle than bare Li cell. The impedance of fresh cells is mainly attributable to the internal contact resistance considering the electrode has not undergone any electrochemical reactions [63]. By Z-view software fitting, the charge transfer resistance of MoN_x-Li and MoN-Li cell was determined to be 102 Ω and 198 Ω, respectively, which

14

is higher than the 58 Ω of bare Li. This result is consistent with the high overpotentials of MoN_x-Li and MoN-Li symmetric cells at initial cycles, possibly due to the extended charge transport path through the MoN_x and MoN artificial interlayer on Li metal surface [32]. When the electrode was cycled at 2 mA cm^{-2} for 100 times, two semicircles are observed in the EIS spectra (**Figure 2d)**. The first semicircle at high frequency is attributable to the SEI/electrode interfacial resistance (R_{surf}) while the second at low frequencies is referring to the charge transfer (CT)/electrical double layer (EDL) resistance (R_{ct}) (**Figure S13**, Supporting Information) [32, 64]. The R_{surf} of MoN_x-Li and MoN-Li cell was fitted as 2.5 Ω and 4.4 Ω, respectively, which is much lower than the 8.5 Ω for the cycled bare Li cell. Previous reports suggest that because the complex characteristics of the multilayer interface between electrolyte and electrode, these two parts can be composed into multiple Resistor-Capacitance (RC) circuits [32, 65]. The data of this work shows two different mechanisms that may correspond to the overlay of the RC circuits, which make CT/EDL and SEI/electrolyte interactions distinguishable [32, 65]. Compared to bare Li cells, the MoN_x-Li cells after 100 cycles displayed a considerably lower SEI/electrode impedance due to the formation of high ion-conductivity of Li_3N-rich layer during Li plating/stripping [63, 66], while the trend of CT/EDL characteristics is basically the same. Given the trivial interfacial resistance of MoN_x-Li, the significantly decreased overpotential of MoN_x-Li should be dominantly contributed by the amended interface between SEI and MoN_x-Li.

3.3 Fundamental understanding of the improved performance

In order to elucidate the mechanisms behind the dramatically improved Li stripping/plating performance, we also performed SEM and XPS post-mortem analyses. SEM characterizations for the bare Li, MoN-Li anodes and MoN_x-Li anodes before and after cycling are shown in **Figure 3**

and **Figure S14**. **Figure 3a** and **3d** are the top and cross-section images of the fresh Li anode, showing a smooth fish scale surface. After 100 cycles, intensive cracks and particles are clearly observed on surface (**Figure 3b**), which is ascribed to the inhomogeneous nucleation and deposition of Li metal, the continuous shedding and reconstructing of unstable SEI and Li dendrite [33]. As a reference, the cycled MoN-Li (**Figure S14**) exhibits alleviative cracks and particles. In contrast, the cycled MoN_x-Li (**Figure 3c**) manifests a smooth and compact surface, demonstrating highly reversible Li metal striping/plating accomplished by the chemically and mechanically approving MoN_x skin. The cross-section observations of cycled electrodes show a thick dead and dendrite Li layer cumulated on bare Li (**Figure 3e**), whereas a steady and interconnected interfacial layer (to be identified as Li_3N and Mo phases by XPS analyses later) on the MoN_x-Li surface (**Figure 3f**).

To clarify the chemical information of SEI layers on cycled MoN_x-Li electrode, XPS characterizations were carried out in inert atmosphere. The N 1s spectrum (**Figure 3g**) shows an intense peak at 398.5 eV, implying the formation of Li_3N component during cycling [25, 67]. The residual deconvoluted peaks centered at 397.4 eV and 400.1 eV are assigned to the N−Mo bond [68], and −NO [69], respectively. **Figure 3h** reveals the Li−N bond at 55.1 eV in Li 1s spectrum, again indicating the formation of Li_3N phase in the MoN_x-Li interface layer [67, 70-73]. For the Mo 3d spectrum (**Figure 3i**), apart from the peaks corresponding to pristine MoN_x (229.6/232.6 eV and 228.8/231.9 eV) [49-53], two new peaks at 227.5/230.5 eV are indexed to $3d_{5/2}$ and $3d_{3/2}$ of metallic Mo [48, 74]. The formation of Li_3N and metallic Mo phases can be interpreted as $MoN_x + 3x Li \rightarrow Mo + x Li_3N$ during Li stripping/plating process, consistent with previous studies [72, 73, 75]. The Li_3N compound was identified with high Li ionic conductivity ($\approx 2 \times 10^{-4}$ S cm^{-1} at 20 °C) [71, 76], which would promote rapid Li-ion diffusion, thus leading to the excellent rate capability and low

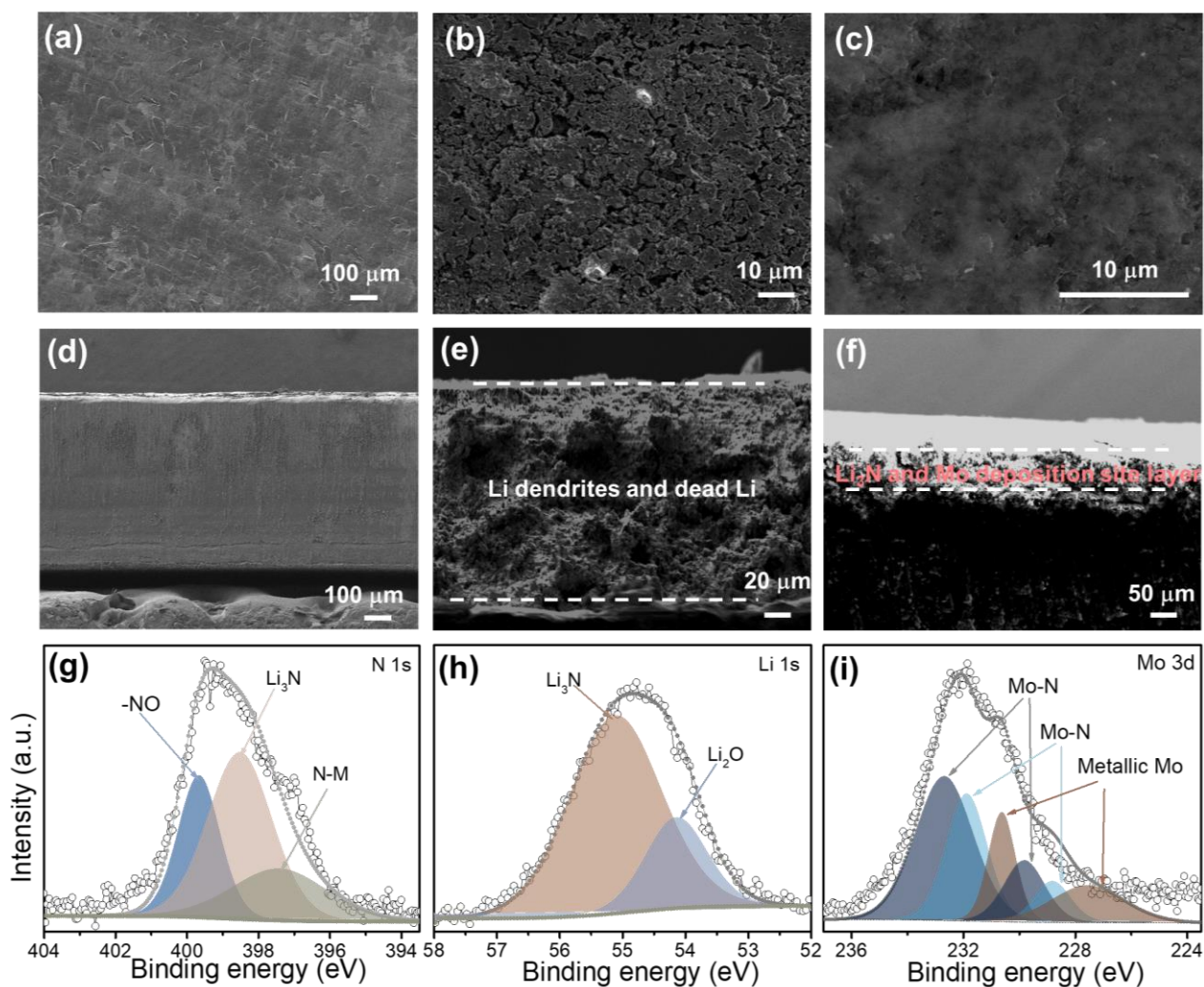overpotentials for MoN$_x$-Li anode.

Figure 3 SEM images of the Li metal anode before and after cycling. SEM images of bare Li metal before cycle (a, d), cycled bare Li metal (b, e), cycled MoN$_x$-Li anode (c, f), deconvoluted N 1s (g), Li 1s (h) and Mo 3d (i) spectra of MoN$_x$-Li after 100 cycles at 2.0 mA cm^{-2} current density with 1.0 mAh cm^{-2} cycle capacity.

The role of *in-situ* formed metallic Mo phase was interpreted by density functional theory (DFT) calculations (see details in Supporting Information). **Figure 4**a and **4b** show the thermodynamically stable configurations of Mo (100) and Li (100) atomic layers. The adsorption energy of Li$^+$ on the top of Mo layer (-0.51 eV) is much larger than on Li layer (+0.39 eV) (**Figure 4c**), which reveals

that the strong interaction between Mo and Li$^+$ would facilitate the Li deposition during cycling. The Li$^+$ adhesion on the top of Mo and Li atomic layer is displayed in **Figure 4d** and **4e**, respectively. Further, we calculated the crystal orbital Hamiltonian populations (COHP) using LOBSTER program because the COHP can illustrate the nature and intensity of interactions between two atoms of the modulus at the orbital angular momentum level. **Figure 4f** exhibits the relaxed state of a Li monolayer on a semi-bulk Mo (100) slab. The values of COHP for the Mo–Mo, Li–Li, and Li–Mo atomic pairs are -0.70 to -0.86, -0.02 to -0.10, -0.12 to -0.16, respectively (**Figure 4g**), indicating the strong Mo-Mo interatomic bond, relatively weak Li-Li bonds, and strong interfacial atomization between Li and Mo, implying the chemically favorable Li–Mo interactions. In addition, in the Li-Mo system, the COHP value of Li–Li bonding was -0.08 to -0.09 (**Figure 4g**), which further illustrate stronger Li–Mo bonding than that of Li–Li bond. According to the previous work [75], Li and Mo intermetallic compounds are inconceivable to form under conventional condition. It means the strong Li–Mo bond would not cause formation of LiMo$_x$ compounds at the absence of external driving force [75], in return, the strong Mo-Li interaction would favor the nucleation of Li metal aside metallic Mo.

The artificial surface protecting strategy proposed in this work for the uniform plating/stripping of Li and the inhibition of Li dendrite growth by MoN$_x$ coating possesses several unique merits that have not been reported before. First, the lithiophilic MoN$_x$ layer is conformally coated on the surface of Li foil, which can block the side reaction between Li metal and electrolyte components. Second, the MoN$_x$ protective layer endows conductive features including high surface energy, excellent electrolyte wettability and strong mechanical strength, which provides favorable conditions for the uniform plating/stripping of Li [77]. The numerous nanopores on MoN$_x$ nanobelts are also beneficial

to the rapid mass transfer (e.g., Li ions and electrolyte). Third, the *in-situ* formed Li$_3$N-and Mo-phase rich layer with high Li ion conductivity and catalytic activity can regulate the fast and uniform deposition of Li and restrict the growth of Li dendrite [66, 68, 76, 78]. Overall, this work not only provides high reversibility and uniform Li deposition but also offer new insights toward the role of MoN$_x$ interface at atomic level.
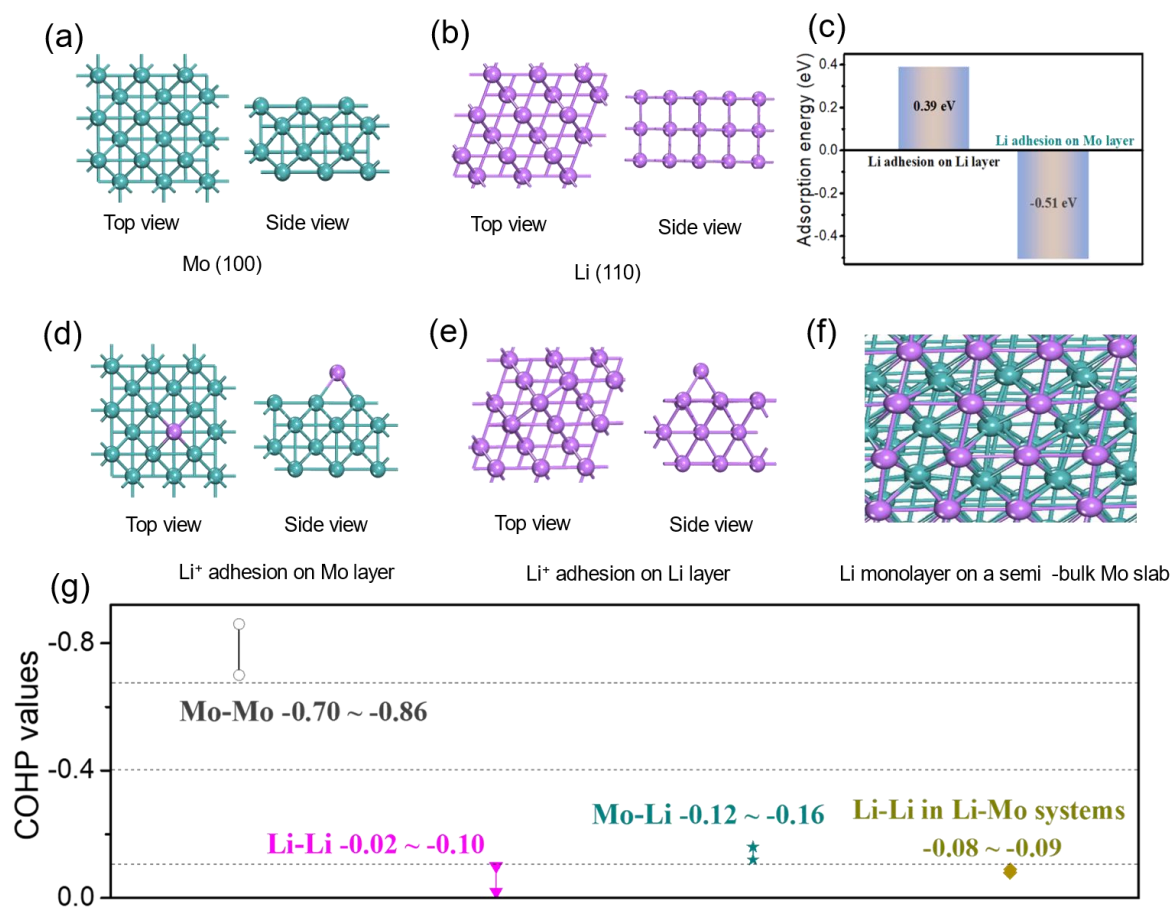

Figure 4 Calculated configurations of Mo (100) (a) and Li (100) (b) atomic Layer; the values of absorption energy of Li ion on Li and Mo atomic layers (c); Li$^+$ adhesion on top of Mo (d) and Li (e) atomic layers; Relaxed state of a Li monolayer on a semi-bulk Mo slab (f, the strength of the interatomic orbital overlaps is stated according to the value of the crystal orbital Hamilton population (COHP)), and COHP values of Mo–Mo, Li–Li, Mo–Li atomic pairs and Li–Li bonding in the Li-Mo system (g) (the molybdenum and lithium atoms are marked with green and pink, respectively).

3.4 MoN$_x$-Li//LiFePO$_4$ full cells

To investigate the practical application of MoN$_x$-Li anode in full cell system, MoN$_x$-Li//LFP and Li//LFP cells were constructed using 1 M LiPF$_6$ in ethylene carbonate/diethyl carbonate (EC/DEC) electrolyte (**Figure 5**). **Figure 5a** and **5b** are the typical charge-discharge profiles of the full cells at 1C (1C= 170 mA g^{-1}) for 500 cycles. The voltage profiles indicated MoN$_x$-Li//LFP with much smaller polarizations than the Li//LFP during cycling, manifesting the reduced charge transfer resistance and high stability of the Li-MoN$_x$ anode. The specific capacities of MoN$_x$-Li//LFP and Li//LFP full cells after the 10th, 50th, 100th, 200th, 400th, and 500th cycles are plotted in **Figure 5c**. Apparently, MoN$_x$-Li//LFP full cell provides a much higher capacity retention of 82.3% than the 1.5% for Li//LFP after 500 cycles. To further compare the high-rate performance, the MoN$_x$-Li//LFP, MoN-Li//LFP and Li//LFP full cells were cycled at 1 C for 500 cycles (**Figure 5d, S15a**) and 3C for 425 cycles (**Figure 5e, S15b**). In **Figure 5d**, it can be observed that the MoN$_x$-Li//LFP cell presents a high specific capacity of 121.3 mAh g^{-1} at the 2nd cycle and 99.9 mAh g^{-1} at the 500th cycle, rendering an extremely low-capacity degradation rate of 0.036% per cycle over 500 cycles. The bare Li//LFP cell exhibits a similarly high capacity of 117 mAh g^{-1} in the 2nd cycle, however, a fast capacity fading was observed after 100 cycles, attributable to the unstable Li metal anode, in agreement with the increasing overpotentials in bare Li//Li symmetric cell measurement (**Figure 2**). Under a higher current rate of 3C (**Figure 5e**), the MoN$_x$-Li//LFP delivers an elevated specific capacity of 70 mAh g^{-1} with 82.3% capacity retention after 425 cycles, further indicating the robust stability of MoN$_x$-Li anode at high power. The average Coulombic efficiencies of the MoN$_x$-Li//LFP full cell remained above 99.3% over 500 cycles at 1C and 99.0% for 425 cycles even at the high rate of 3C. In sharp comparison, the bare Li//LFP full cell displays fluctuating and decreasing Coulombic

efficiencies upon prolonged cycling. **Table S4** (Supporting Information) summarized the full cell performances of this work in comparison to the reported LMBs with modified Li metal anodes. It clearly illustrates the MoN_x-Li//LFP full cell in this work outperform almost all the peers with regard to cycle life and Coulombic efficiencies at a high rate of 1C, suggesting its promising application in high energy LMBs.
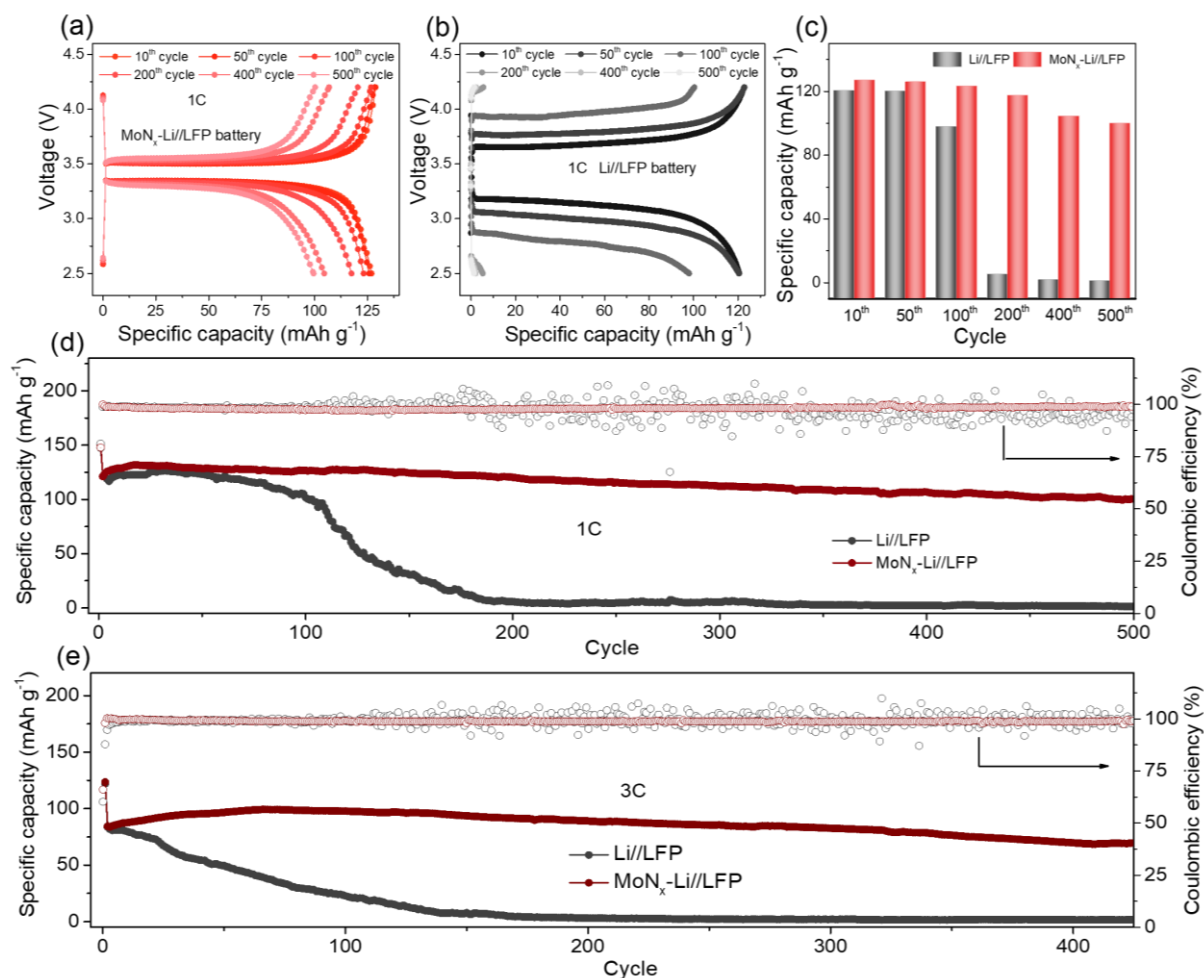

Figure 5 Typical charge/discharge profiles of the MoN_x-Li//LFP (a), bare Li//LFP (b) and specific capacities (c) after different cycles at 1C rate (1C = 170 mA g^{-1}). Long-term cycling stability and Coulombic efficiencies of the bare Li//LFP and MoN_x-Li//LFP full cells at 1C (d) and 3C (e), the first cycle is activated at 0.1C (test at least 5 cells for each condition).

4. Conclusions

In summary, different from the previously reported polymer or oxides interlayer in literature [18, 29-32], a novel lithiophilic Mo_3N_2/MoN heterostructure (MoN_x) as protective layer was developed in this work for dendrite-free Li metal anode. The MoN_x artificial layer exhibits two unique merits: (i) the heterostructural MoN_x interlayer provides appealing properties of enhanced electrolyte wettability, high surface energy, and high mechanical strength, which can effectively inhibit the lithium dendrite growth; (ii) during the lithium stripping/plating process, the MoN_x protective layer could *operando* develop Mo phase and Li_3N-rich layer, providing rich deposition sites and fast ion migration kinetics, further mitigating the polarization and hindering the Li dendrite growth. These findings are demonstrated by a suit of experimental and simulation studies. The MoN_x-Li delivers an ultra-long cycling stability (over more than 2000 h) at 5 mA cm^{-2} with 1 mAh cm^{-2}. Furthermore, the MoN_x-Li//LFP full cells manifest exceptional cyclic stability with 82.3 % capacity retention after 500 cycles at 1C and 82.3% capacity retention after 425 cycles at a high rate of 3C. This intriguing strategy in improving the cycling performance and safety of dendrite-free Li metal batteries in this work paves new path towards developing advanced alkali metal batteries for high-energy storage applications.

Conflicts of interest

The authors declare no competing interests.

References:

[1]   B. Yu, D.X. Yang, Y. Hu, J.R. He, Y.F. Chen, W.D. He, Mo_2C Nanodots anchored on N-doped porous CNT microspheres as electrode for efficient Li-Ion storage, Small Methods 3 (2019) 1800287.

[2]   W.P. Wang, J. Zhang, J. Chou, Y.X. Yin, Y. You, S. Xin, Y.G. Guo, Solidifying cathode-electrolyte interface for lithium-sulfur batteries, Adv. Energ. Mater. 11 (2021) 2000791.

[3]   Y.H. Wang, X.T. Li, We.P. Wang, H.J. Yan, S. Xin, Y.G. Guo, Chalcogen cathode and its conversion electrochemistry in rechargeable Li/Na batteries, Sci. China Chem. 63 (2020) 1402-1415.

[4]   Z.L. Xu, S.J. Kim, D. Chang, K.Y. Park, K.S. Dae, K.P. Dao, J.M. Yuk, K. Kang, Visualization of regulated nucleation and growth of lithium sulfides for high energy lithium sulfur batteries, Energ. Environ. Sci. 12 (2019) 3144-3155.

[5]   Z.L. Xu, J.K. Kim, K. Kang, Carbon nanomaterials for advanced lithium sulfur batteries, Nano Today 19 (2018) 84-107.

[6]   X.B. Cheng, R. Zhang, C.Z. Zhao, Q. Zhang, Toward Safe Lithium Metal Anode in Rechargeable Batteries: A Review, Chem. Rev. 117 (2017) 10403-10473.

[7]   H.Y. Huo, Y. Chen, R.Y. Li, N. Zhao, J. Luo, J.G.P.D. Silva, R. Mücke, P. Kaghazchi, X.X. Guo, X.L. Sun, Design of a mixed conductive garnet/Li interface for dendrite-free solid lithium metal batteries, Energ. Environ. Sci. 13 (2020) 127-134.

[8]   D.C. Lin, Y.Y. Liu, Y. Cui, Reviving the lithium metal anode for high-energy batteries, Nat.

Nanotechnol. 12 (2017) 194-206.

[9] W.P. Wang, J. Zhang, Y.X. Yin, H. Duan, J. Chou, S.Y. Li, M. Yan, S. Xin, Y.G. Guo, A rational reconfiguration of electrolyte for high-energy and long-life lithium-chalcogen batteries, Adv. Mater. 32 (2020) 2000302.

[10] S.Z. Niu, S.W. Zhang, R. Shi, J.W. Wang, W.J. Wang, X.M. Chen, Z.Q. Zhang, J. Miao, A. Amini, Y.S. Zhao, C. Cheng, Freestanding agaric-like molybdenum carbide/graphene/N-doped carbon foam as effective polysulfide anchor and catalyst for high performance lithium sulfur batteries, Energ. Storage Mater. 33 (2020) 73-81.

[11] B. Liu, J.G. Zhang, W. Xu, Advancing Lithium Metal Batteries, Joule 2 (2018) 833-845.

[12] B. Yu, D.J. Chen, Z.G. Wang, F. Qi, X.J. Zhang, X.Q. Wang, Y. Hu, B. Wang, W.L. Zhang, Y.F. Chen, J.R. He, W.D. He, Mo_2C quantum dots@graphene functionalized separator toward high-current-density lithium metal anodes for ultrastable Li-S batteries, Chem. Eng. J. 399 (2020) 125837.

[13] B. Yu, Y.F. Chen, Z.G. Wang, D.J. Chen, X.Q. Wang, W.L. Zhang, J.R. He, W.D. He, $1T-MoS_2$ nanotubes wrapped with N-doped graphene as highly-efficient absorbent and electrocatalyst for Li-S batteries, J. Power Sources 447 (2020) 227364.

[14] X.J. Zhang, Y.F. Chen, B. Yu, B. Wang, X.Q. Wang, W.L. Zhang, D.X. Yang, J.R. He, Lithiophilic 3D VN@N-rGO as a multifunctional interlayer for dendrite-free and ultrastable lithium-metal batteries, ACS Appl. Mater. Inter. 13 (2021) 20125-20136.

[15] S.Z. Niu, S.W. Zhang, D.Y. Li, X. Wang, X.M. Chen, R. Shi, N. Shen, M.T. Jin, X. Zhang, Q. Lian, R.Q. Huang, A. Amini, Y.S. Zhao, C. Cheng, Sandwiched Li plating between Lithiophilic-lithiophobic gradient silver@fullerene interphase layer for ultrastable lithium metal anodes, Chem. Eng. J. 429 (2022) 132156.

[16]Q.F. Yang, C.L. Li, Li metal batteries and solid-state batteries benefiting from halogen-based strategies, Energ. Storage Mater. 14 (2018) 100-117.

[17]M.D. Tikekar, S. Choudhury, Z.Y. Tu, L.A. Archer, Design principles for electrolytes and interfaces for stable lithium-metal batteries, Nat. Energ. 1 (2016).

[18]Z.X. Zhou, Y.Y. Feng, J.L. Wang, B. Liang, Y.H. Li, Z.X. Song, D.M. Itkis, J.X. Song, A robust, highly stretchable ion-conducive skin for stable lithium metal batteries, Chem. Eng. J. 396 (2020) 125254.

[19]R. Zhang, N.W. Li, X.B. Cheng, Y.X. Yin, Q. Zhang, Y.G. Guo, Advanced micro/nanostructures for lithium metal anodes, Adv. Sci. 4 (2017) 1600445.

[20]J.L. Wang, F. Ding, W. Xu, Lithium metal anodes for rechargeable batteries, Energ. Environ. Sci. 7 (2014) 513.

[21]X. Wang, R.Q. Huang, S.Z. Niu, L. Xu, Q.C. Zhang, A. Amini, C. Cheng, Research progress on graphene-based materials for high-performance lithium-metal batteries, New Carbon Mater. 36 (2021) 711-728.

[22]J.R. He, A. Manthiram, 3D CoSe@C aerogel as a host for dendrite-free lithium-metal anode and efficient sulfur cathode in Li-S full cells, Adv. Energ. Mater. 10 (2020) 2002654.

[23]J.R. He, A. Manthiram, Long-life, high-rate lithium-sulfur cells with a carbon-free VN host as an efficient polysulfide adsorbent and lithium dendrite inhibitor, Adv. Energ. Mater. 10 (2020) 1903241.

[24]J.R. He, A. Bhargav, W. Shin, A. Manthiram, Stable dendrite-free sodium-sulfur batteries enabled by a localized high-concentration electrolyte, JACS (2021) https://doi.org/10.1021/jacs. 1c08851.

[25] Q.Y. Dong, B. Hong, H.L. Fan, H. Jiang, K. Zhang, Y.Q. Lai, Inducing the formation of in situ Li_3N-rich SEI via nanocomposite Plating of Mg_3N_2 with lithium enables high-performance 3D lithium-metal batteries, ACS. Appl. Mater. Inter 12 (2019) 627-636.

[26] C.Z. Wang, A.X. Wang, L.X. Ren, X.Z. Guan, D.H. Wang, A.P. Dong, C.Y. Zhang, G.J. Li, J.Y. Luo, Controlling Li Ion Flux through Materials Innovation for Dendrite-Free Lithium Metal Anodes, Adv. Funct. Mater. 29 (2019) 1905940.

[27] Y. Zhao, L.V. Goncharova, Q. Sun, X. Li, A. Lushington, B.Q. Wang, R.Y. Li, F. Dai, M. Cai, X.L. Sun, Robust metallic lithium anode protection by the molecular-layer-deposition technique, Small Methods 2 (2018) 1700417.

[28] Z. Liang, G.Y. Zheng, C. Liu, N. Liu, W.Y. Li, K. Yan, H.B. Yao, P.C. Hsu, S. Chu, Y. Cui, Polymer nanofiber-guided uniform lithium deposition for battery electrodes, Nano Lett. 15 (2015) 2910-2916.

[29] H.M. Zhang, X.B. Liao, Y.P. Guan, Y. Xiang, M. Li, W.F. Zhang, X.Y. Zhu, H. Ming, L. Lu, J.Y. Qiu, Y.Q. Huang, G.P. Cao, Y.S. Yang, L.Q. Mai, Y. Zhao, H. Zhang, Lithiophilic-lithiophobic gradient interfacial layer for a highly stable lithium metal anode, Nat. Commun. 9 (2018).

[30] J.J. Yang, C.J. Hu, Y. Jia, Y.C. Pang, L. Wang, W. Liu, X.M. Sun, Surface restraint synthesis of an organic-inorganic hybrid layer for dendrite-free lithium metal anode, ACS Appl. Mater. Inter. 11 (2019) 8717-8724.

[31] J. Luo, C.C. Fang, N.L. Wu, High polarity poly(vinylidene difluoride) thin coating for dendrite-free and high-performance lithium metal anodes, Adv. Energy Mater. 8 (2018) 1701482.

[32] E. Kazyak, K.N. Wood, N.P. Dasgupta, Improved cycle life and stability of lithium metal anodes through ultrathin atomic layer deposition surface treatments, Chem. Mater. 27 (2015) 6457-

6462.

[33] K. Chen, R. Pathak, A. Gurung, E.A. Adhamash, B. Bahrami, Q.Q. He, H. Qiao, A.L. Smirnova, J.J. Wu, Q.Q. Qiao, Y. Zhou, Flower-shaped lithium nitride as a protective layer via facile plasma activation for stable lithium metal anodes, Energ. Storage Mater. 18 (2019) 389-396.

[34] J.L. Yang, S.X. Zhao, Y.M. Lu, X.T. Zeng, W. Lv, G.Z. Cao, In-situ topochemical nitridation derivative MoO_2-Mo_2N binary nanobelts as multifunctional interlayer for fast-kinetic Li-sulfur batteries, Nano Energ. 68 (2020) 104356.

[35] G.L. Liu, L.F. Xu, Y.Q. Li, D.L. Guo, N.T. Wu, C.Z. Yuan, A.M. Qin, A. Cao, X.M. Liu, Metal-organic frameworks derived anatase/rutile heterostructures with enhanced reaction kinetics for lithium and sodium storage, Chem. Eng. J. 430 (2022) 132689.

[36] P. Du, L. Cao, B. Zhang, C.H. Wang, Z.M. Xiao, J.F. Zhang, D. Wang, X. Ou, Recent progress on heterostructure materials for next-generation sodium/potassium ion batteries, Renew. Sustain. Energ. Rev. 151 (2021) 111640.

[37] W.B. Li, Q.Q. Song, M. Li, Y.F. Yuan, J.H. Zhang, N. Wang, Z.H. Yang, J.F. Huang, J. Lu, X.F. Li, Chemical heterointerface engineering on hybrid electrode materials for electrochemical energy storage, Small Methods 5 (2021) 2100444.

[38] K. Chang, W. Chen, L-cysteine-assisted synthesis of layered MoS_2/graphene composites with excellent electrochemical performances for lithium ion batteries, ACS Nano 5 (2011) 4720-4728.

[39] C. He, J.H. Zhang, W.X. Zhang, T.T. Li, GeSe/BP van der Waals heterostructures as promising anode materials for potassium-ion batteries, J. Physical Chemistry. C 123 (2019) 5157-5163.

[40] Q.L. Wu, S.X. Zhao, L. Yu, X.X. Zheng, Y.F. Wang, L.Q. Yu, C.W. Nan, G.Z. Cao, Oxygen vacancy-enriched MoO_{3-x} nanobelts for asymmetric supercapacitors with excellent room/low

temperature performance, J. Mater. Chem. A 7 (2019) 13205-13214.

[41] Y. Xu, R. Wu, J.F. Zhang, Y.M. Shi, B. Zhang, Anion-exchange synthesis of nanoporous FeP nanosheets as electrocatalysts for hydrogen evolution reaction, Chem. Commun. 49 (2013) 6656.

[42] Y.F. Yu, J. Zhang, X. Wu, W.W. Zhao, B. Zhang, Nanoporous single-crystal-like $Cd_xZn_{1-x}S$ nanosheets fabricated by the cation-exchange reaction of inorganic-organic hybrid zns-amine with cadmium ions, Angew. Chemie Internat. Edition 51 (2012) 897-900.

[43] T.S. Wang, X.B. Liu, X.D. Zhao, P.G. He, C.W. Nan, L.Z. Fan, Regulating uniform li plating/stripping via dual-conductive metal-organic frameworks for high-rate lithium metal batteries, Adv. Funct. Mater. 30 (2020) 2000786.

[44] J.R. He, W.Q. Lv, Y.F. Chen, J. Xiong, K.C. Wen, C. Xu, W.L. Zhang, Y.R. Li, W. Qin, W.D. He, Three-dimensional hierarchical C-Co-N/Se derived from metal-organic framework as superior cathode for Li-Se batteries, J. Power Sources 363 (2017) 103-109.

[45] X.Q. Wang, J.R. He, B. Yu, B.C. Sun, D.X. Yang, X.J. Zhang, Q.H Zhang, W.L. Zhang, L. Gu, Y.F. Chen, $CoSe_2$ nanoparticles embedded MOF-derived Co-N-C nanoflake arrays as efficient and stable electrocatalyst for hydrogen evolution reaction, Appl. Catal. B: Environ. 258 (2019) 117996.

[46] J.B. Wang, C.Y. Yang, J.J. Wang, L.J. Han, M.D. Wei, Two-dimensional MoN@N-doped carbon hollow spheres as an anode material for high performance lithium-ion battery, Electrochim. Acta 295 (2019) 246-252.

[47] X. Shi, A.P. Wu, H.J. Yan, L. Zhang, C.G. Tian, L. Wang, H.G. Fu, A "MOFs plus MOFs" strategy toward $Co-Mo_2N$ tubes for efficient electrocatalytic overall water splitting, J. Mater. Chem. A 6 (2018) 20100-20109.

[48] K. Inumaru, K. Baba, S. Yamanaka, Synthesis and characterization of superconducting $\beta-Mo_2N$

Crystalline phase on a Si substrate: an application of pulsed laser deposition to nitride chemistry, Chem. Mater. 17 (2005) 5935-5940.

[49] G.T. Kim, T.K. Park, H. Chung, Y.T. Kim, M.H. Kwon, J.G. Choi, Growth and characterization of chloronitroaniline crystals for optical parametric oscillators: I. XPS study of Mo-based compounds, Appl. Surf. Sci. 152 (1999) 35-43.

[50] C. Shi, A.M. Zhu, X.F. Yang, C.T. Au, On the catalytic nature of VN, Mo_2N, and W_2N nitrides for NO reduction with hydrogen, Appl. Catal. A: General 276 (2004) 223-230.

[51] D. Mckay, J.S.J. Hargreaves, R.F. Howe, XPS evidence for molybdenum nitride formation in ZSM-5, Catal. Lett. 112 (2006) 109-113.

[52] C.C. Wang, L.L. Song, Y.N. Zou, Excellent hardness property of bulk MoN fabricated by a novel method, Results Phys 19 (2020) 103362.

[53] Y.B. Ting, H.R. Wu, N.P. Kherani, K. Lian, Development of pseudocapacitive molybdenum oxide-nitride for electrochemical capacitors, Mater. Chem. Phys. 154 (2015) 118-124.

[54] T. Wang, G.J. Zhang, S. Ren, B.L. Jiang, Effect of nitrogen flow rate on structure and properties of MoN_x coatings deposited by facing target sputtering, J. Alloy. Compd 701 (2017) 1-8.

[55] H. Park, S. Vadahanambi, Carbon sheathed molybdenum nitride nanoparticles anchored on reduced graphene oxide as high-capacity sodium-ion battery anodes and supercapacitors, New J. Chem 42 (2018) 5668.

[56] Y.L. Jiang, J. Dong, S.S. Tan, Q.L. Wei, F.Y. Xiong, W. Yang, Y.H. Shen, Q.X. Zhang, Z.A. Liu, Q.Y. An, L.Q. Mai, Surface pseudocapacitance of mesoporous Mo_3N_2 nanowire anode toward reversible high-rate sodium-ion storage, J. Energ. Chem 55 (2021) 295-303.

[57] M. Jäckle, A. Groß, Microscopic properties of lithium, sodium, and magnesium battery anode

materials related to possible dendrite growth, J. Chemical Physics 141 (2014) 174710.

[58]C. Ling, D. Banerjee, M. Matsui, Study of the electrochemical deposition of Mg in the atomic level: Why it prefers the non-dendritic morphology, Electrochim. Acta 76 (2012) 270-274.

[59]A. Ferrese, J. Newman, Mechanical deformation of a lithium-metal anode due to a very stiff separator, J. Electrochem. Soc. 161 (2014) A1350-A1359.

[60]Y.G. Lee, S. Ryu, T. Sugimoto, T. Yu, W. Chang, Y. Yang, C. Jung, J. Woo, S.G. Kang, H.N. Han, S.G. Doo, Y. Hwang, H. Chang, J.M. Lee, J.Y. Sun, Dendrite-free lithium deposition for lithium metal anodes with interconnected microsphere protection, Chem. Mater. 29 (2017) 5906-5914.

[61]M.H. Ryou, Y.M. Lee, Y.J. Lee, M. Winter, P. Bieker, Mechanical surface modification of lithium metal: towards improved li metal anode performance by directed li plating, Adv. Funct. Mater. 25 (2015) 834-841.

[62]Y.F. Feng, C.F. Zhang, X.X. Jiao, Z.X Zhou, J.X. Song, Highly stable lithium metal anode with near-zero volume change enabled by capped 3D lithophilic framework, Energ. Storage Mater. 25 (2020) 172-179.

[63]Q. Li, S.P. Zhu, Y.Y. Lu, 3D porous Cu current collector/Li-metal composite anode for stable lithium-metal batteries, Adv. Funct. Mater. 27 (2017) 1606422.

[64]S.S. Zhang, K. Xu, T.R. Jow, EIS study on the formation of solid electrolyte interface in Li-ion battery, Electrochim. Acta 51 (2006) 1636-1640.

[65]D. Aurbach, Review of selected electrode-solution interactions which determine the performance of Li and Li ion batteries, J. Power Sources 89 (2000) 206-218.

[66]M. Baloch, D. Shanmukaraj, O. Bondarchuk, E. Bekaert, T. Rojo, M. Armand, Variations on

Li$_3$N protective coating using ex-situ and in-situ techniques for Li$^+$ in sulphur batteries, Energ. Storage Mater. 9 (2017) 141-149.

[67] Z.L. Hu, S. Zhang, S.M. Dong, W.J. Li, H. Li, G.L. Cui, L.Q. Chen, Poly(ethyl α-cyanoacrylate)-based artificial solid electrolyte interphase layer for enhanced interface stability of Li metal anodes, Chem. Mater. 29 (2017) 4682-4689.

[68] X.F. Bian, Q. Pang, Y.J. Wei, D. Zhang, Y. Gao, G. Chen, Dual Roles of Li$_3$N as an electrode additive for li-excess layered cathode materials: a li-ion sacrificial salt and electrode-stabilizing agent, Chemistry-A European J. 24 (2018) 13815-13820.

[69] Y. Luo, T.Y. Li, H.Z. Zhang, W. Liu, X.B. Zhang, J.W. Yan, H.M. Zhang, X.F. Li, Endogenous symbiotic Li$_3$N/cellulose skin to extend the cycle life of lithium anode, Angew. Chemie Internat. Edition 60 (2021) 11718-11724.

[70] L. Fan, H.L. Zhuang, L.N. Gao, Y.Y. Lu, L.A. Archer, Regulating Li deposition at artificial solid electrolyte interphases, J. Mater. Chem. A 5 (2017) 3483-3492.

[71] G. Gu, K. Wang, N. Xiong, Z. Li, Z. Fan, S. Hu, X. Zou, Template free synthesis of lithium doped three-dimensional macroporous graphitic carbon nitride for photocatalytic N$_2$ fixation: the effect of Li-N active sites, Dalton Trans. 48 (2019) 5083-5089.

[72] J. Ma, L. Yu, Z.W. Fu, Electrochemical and theoretical investigation on the reaction of transition metals with Li$_3$N, Electrochim. Acta 51 (2006) 4802-4814.

[73] K.N. Wood, G. Teeter, XPS on Li-battery-related compounds: analysis of inorganic SEI phases and a methodology for charge correction, ACS Appl. Energ. Mater. 1 (2018) 4493-4504.

[74] A. Kocijan, I. Milosev, B. Pihlar, Cobalt-based alloys for orthopaedic applications studied by electrochemical and XPS analysis, J. Mater. Sci. Mater. Med. 15 (2004) 643-650.

[75]L. Luo, J.Y. Li, H. Yaghoobnejad Asl, A. Manthiram, A 3D lithiophilic Mo_2N-modified carbon nanofiber architecture for dendrite-free lithium-metal anodes in a full cell, Adv. Mater. 31 (2019) 1904537.

[76]K. Park, B.C. Yu, J.B. Goodenough, Li_3N as a cathode additive for high-energy-density lithium-ion batteries, Adv. Energ. Mater. 6 (2016) 1502534.

[77]P.C. Zou, Y.M. Sui, H.C. Zhan, C.Y. Wang, H.L. L. Xin, H.M. Cheng, F.Y. Kang, C. Yang, Polymorph evolution mechanisms and regulation strategies of lithium metal anode under multiphysical fields, Chem. Rev. 121 (2021) 5986-6056.

[78]S.F. Liu, X.H. Xia, Y. Zhong, S.J. Deng, Z.J. Yao, L.Y. Zhang, X.B. Cheng, X.L. Wang, Q. Zhang, J.P. Tu, 3D TiC/C core/shell nanowire skeleton for dendrite-free and long-life lithium metal anode, Adv. Energ. Mater. 8 (2018) 1702322.